NEUROSCIENCE

Increased vesicle fusion competence underlies long-term potentiation at hippocampal mossy fiber synapses

Ryota Fukaya[1,2]†, Himawari Hirai[1]†, Hirokazu Sakamoto[3]†, Yuki Hashimotodani[1]*, Kenzo Hirose[3,4]*, Takeshi Sakaba[1]*

Presynaptic long-term potentiation (LTP) is thought to play an important role in learning and memory. However, the underlying mechanism remains elusive because of the difficulty of direct recording during LTP. Hippocampal mossy fiber synapses exhibit pronounced LTP of transmitter release after tetanic stimulation and have been used as a model of presynaptic LTP. Here, we induced LTP by optogenetic tools and applied direct presynaptic patch-clamp recordings. The action potential waveform and evoked presynaptic Ca^{2+} currents remained unchanged after LTP induction. Membrane capacitance measurements suggested higher release probability of synaptic vesicles without changing the number of release-ready vesicles after LTP induction. Synaptic vesicle replenishment was also enhanced. Furthermore, stimulated emission depletion microscopy suggested an increase in the numbers of Munc13-1 and RIM1 molecules within active zones. We propose that dynamic changes in the active zone components may be relevant for the increased fusion competence and synaptic vesicle replenishment during LTP.

INTRODUCTION

Synapses are sites of neuronal communication between neurons. Synaptic transmission is initiated by action potentials (APs) arriving at the presynaptic terminals. An AP induces presynaptic Ca^{2+} influx and triggers neurotransmitter release via exocytosis of readily releasable vesicles, causing postsynaptic responses. The amounts of transmitter release can vary depending on the preceding neuronal activities, thereby modulating the strength and temporal dynamics of synaptic transmission (*1*–*4*). Presynaptic long-term potentiation (LTP) is a form of plasticity induced by intense neuronal activities, where the amounts of transmitter release are upscaled over tens of minutes (*5*). Presynaptic LTP is believed to play a fundamental role in learning and memory across animals (*6*–*8*).

The synapse between a hippocampal mossy fiber (hMF) and a CA3 pyramidal cell (a MF-CA3 synapse) has been used as a model for presynaptic LTP (mfLTP) (*9*). Tetanic stimulation of the dentate gyrus (DG) granule cells (GCs) induces long-lasting potentiation of glutamate release from hMF boutons (hMFBs), the presynaptic terminals of GCs, in a cyclic adenosine monophosphate (cAMP)/protein kinase A (PKA)–dependent manner (*10*–*12*). The mfLTP involves changes in electrophysiological membrane properties and/or molecular release machinery in presynaptic active zones (AZs), which can regulate the number of vesicles in the readily releasable pool (RRP) and/or release probability (Pr) for vesicles in the RRP. In hMFBs, presynaptic hyperpolarization-activated cyclic nucleotide–gated cation (HCN) channels are modulated upon the mfLTP (*13*), although this is a matter of debate (*14*). Some other studies have identified candidate release-related proteins responsible for mfLTP using genetics (*15*–*19*). However, the mechanisms underlying mfLTP remain largely unknown.

MF-CA3 synapses are characterized by a large presynaptic terminal (~5 μm), allowing one to apply direct presynaptic patch-clamp recordings and to dissect the release mechanisms (*20*, *21*). In this study, we introduced an optogenetic technique to MF-CA3 synapses and induced mfLTP with tetanic stimulation using light illumination. We could directly examine the changes in membrane properties and the release mechanisms following LTP induction by applying presynaptic patch-clamp recordings to light-sensitive hMFBs. We revealed that Pr of the vesicles within the RRP became higher after LTP induction without changing the RRP size. Furthermore, stimulated emission depletion (STED) microscopy suggested an increase in the number of Munc13-1 and RIM1 molecules in the AZs, which are important regulators of vesicle recruitment and fusion competence.

RESULTS

The optical tetanic stimulation induced presynaptic LTP at the MF-CA3 synapses

Optogenetic tools have been used to evoke synaptic responses at the MF-CA3 synapses in hippocampal slice preparations (*19*, *22*–*24*). In this study, we introduced them to MF-CA3 synapses and induced mfLTP with light-evoked APs (Fig. 1). This approach has the following advantages over electrical stimulation. (i) The expression of photoactivated cation channels in GCs allows one to stimulate MFs selectively. (ii) Photosensitive responses and fluorescent tags allow reliable identification of the stimulated terminals (Figs. 2 to 5).

To optically induce mfLTP, Chronos, a fast version of channelrhodopsin-2 (*25*), was tagged with green fluorescent protein (GFP) and expressed in GCs by injection of adeno-associated viruses (AAVs) into the DG (Fig. 1A). Using blue light illumination in the DG, we successfully recorded field potentials at the stratum lucidum, a location where MFs contact the CA3 pyramidal cells

[1]Graduate School of Brain Science, Doshisha University, Kyotanabe, Kyoto 610-0394, Japan. [2]Institute of Biology/Genetics, Freie Universität Berlin, 14195 Berlin, Germany. [3]Department of Pharmacology, Graduate School of Medicine, The University of Tokyo, Bunkyo-ku, Tokyo 113-0033, Japan. [4]International Research Center for Neurointelligence (WPI-IRCN), The University of Tokyo, Bunkyo-ku, Tokyo 113-0033, Japan.
*Corresponding author. Email: yhashimo@mail.doshisha.ac.jp (Y.H.); kenzoh@m.u-tokyo.ac.jp (K.H.); tsakaba@mail.doshisha.ac.jp (T.S.)
†These authors contributed equally to this work.

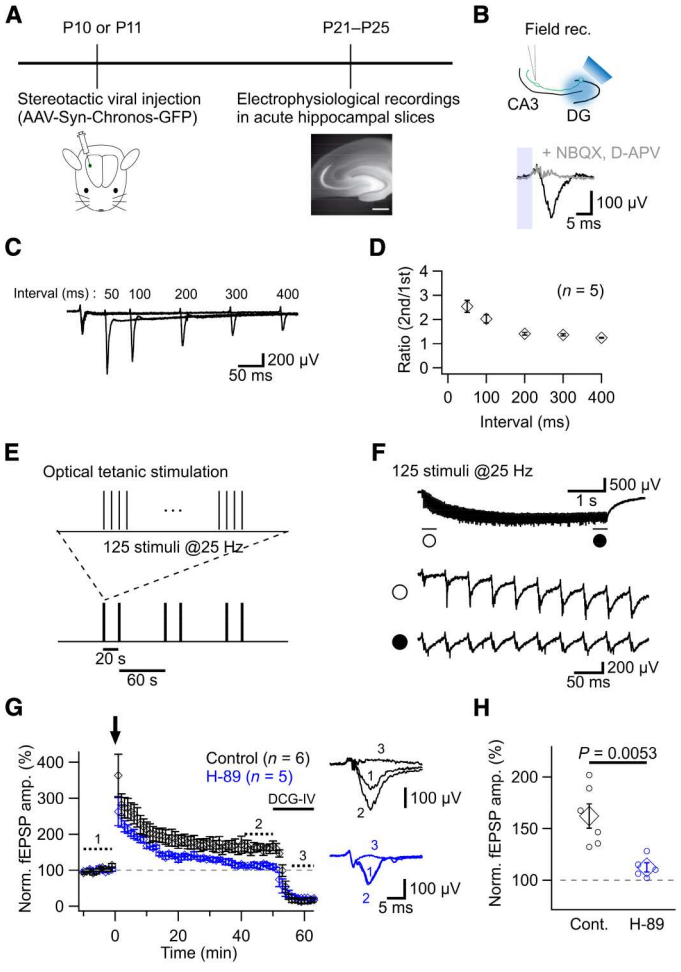

Fig. 1. Optical tetanic stimulation induced LTP at the MF-CA3 synapses. (**A**) The experimental design. AAV (AAV-Syn-Chronos-GFP) was injected into the DG of postnatal day 10 (P10) or P11 rats. Electrophysiological recordings were performed in acute hippocampal slices at P21 to P25. Expression of Chronos-GFP in the DG, hilus, and stratum lucidum was observed. Scale bar, 500 μm. (**B**) Field potentials were recorded in stratum lucidum in response to blue light illumination at DG (top). The light illumination (5 ms; blue shade) evoked field potential (black), which was diminished after the application of NBQX (10 μM) and D-APV (50 μM; gray) (bottom). (**C** and **D**) fEPSPs triggered by paired light stimuli with various intervals (50 to 400 ms) (C). The second fEPSP amplitudes relative to the first ones are plotted against the intervals (D). In (D) and (G), each *n* indicates the number of slices. (**E**) The scheme of optical tetanic stimulation. A pair of the train light stimulations (125 stimuli at 25 Hz, 20-s interval) was applied three times with 60-s intervals. (**F**) Example of the fEPSPs in response to the train light stimulation (125 stimuli at 25 Hz) (top). Responses at the first (open) and the last 10 stimuli (filled) are magnified in the middle and bottom, respectively. (**G**) fEPSPs recorded before and after the optical tetanic stimulation without (black; control) and with H-89 (10 μM) (blue). fEPSP amplitudes are plotted against the time after the optical tetanic stimulation (arrow) (left). DCG-IV (1 μM) was applied at the last 10 min (phase 3). The fEPSP traces for phases 1, 2, and 3 are shown (right). (**H**) fEPSP amplitudes at phase 2 in (G). Values were normalized by the baselines (phase 1). Each circle represents a value for one slice. Statistical significances were assessed with unpaired *t* test.

(Fig. 1B). The evoked response was the glutamatergic field excitatory postsynaptic potential (fEPSP) because it was completely blocked by the application of 2,3-dihydroxy-6-nitro-7-sulfamoylbenzo[*f*]-quinoxaline (NBQX) and D-aminophosphovalerate (D-APV), blockers of AMPA/kainate and *N*-methyl-D-aspartate (NMDA) receptors, respectively (Fig. 1B, bottom). When we applied paired-pulse light illumination with an interval of 50 ms, the fEPSPs showed pronounced paired-pulse facilitation (Fig. 1, C and D). Facilitation was attenuated with longer intervals (Fig. 1, C and D), exhibiting a known feature of MF-CA3 synapses (*19*, *26*). In addition, light-evoked fEPSPs were inhibited by the application of (2S,2'R,3'R)-2-(2',3'-Dicarboxycyclopropyl)glycine (DCG-IV), an agonist of group II metabotropic glutamate receptors that preferentially inhibits MF-CA3 responses (Fig. 1G) (*27*). These results ensured that light illumination at the DG evoked MF-CA3 synaptic responses.

To induce mfLTP, we delivered optical tetanic stimulation (three bursts of a pair of 125 pulses at 25 Hz separated by 20 s; Fig. 1E). We confirmed that synchronized synaptic responses were reliably evoked throughout the tetanic stimulation (Fig. 1F). Using this LTP induction protocol, the fEPSPs were amplified ~3.5-fold at their maximum, gradually decreased, but showed sustained potentiation (162 ± 12% of the baseline at 40 to 50 min after the induction; $n = 6$ slices; Fig. 1, G and H), indicating that mfLTP was induced. The mfLTP is expressed presynaptically in a PKA-dependent manner (*10*, *11*). We observed an 18 ± 6% decrease in paired-pulse facilitation after mfLTP induction ($n = 6$ slices; $P = 0.036$, paired *t* test), suggesting an increase of Pr. The decrease was smaller than previous studies (*5*, *18*), possibly because of a difference in the induction protocol or the external Ca^{2+} concentration. Furthermore, 10 μM H-89, a cell-permeable PKA inhibitor, suppressed optically induced LTP (Fig. 1, G and H). Together, we succeeded in optically inducing mfLTP.

AP waveforms were not changed after LTP induction

We addressed the underlying mechanisms of mfLTP by applying direct presynaptic patch-clamp recordings to the hMFBs combined with optical LTP induction (Figs. 2 and 3). In the following electrophysiological experiments, we used Chronos-(+) hMFBs without tetanic stimulation as a control and compared them with Chronos-(+) hMFBs that underwent tetanic stimulation.

Figure 2A shows how to record from the hMFBs after optical tetanic stimulation. Light-evoked fEPSPs were monitored at the stratum lucidum, before and after the optical tetanic stimulation. As described above, fEPSPs were amplified approximately fourfold immediately after tetanic stimulations [post-tetanic potentiation (PTP)], which returned to approximately two times of the baseline (Fig. 2B). In Fig. 1G, the ~1.5-fold amplification persisted afterward, which presumably reflected LTP. After the PTP phase, we performed whole-cell patch-clamp recordings in the Chronos-(+) hMFBs, which showed an inward current locked to light illumination under voltage-clamp configurations (Fig. 2C). We performed the presynaptic recordings 10 to 60 min following the LTP induction (see figs. S2 and S6).

At MF-CA3 synapses, glutamate release induced by APs is influenced by the level of preceding resting membrane potential (RMP) (*28*). In addition, the broadening of presynaptic AP waveforms in hMFBs increases the Ca^{2+} current per AP and amplifies glutamate release (*20*). During the repetitive optical stimulation, APs

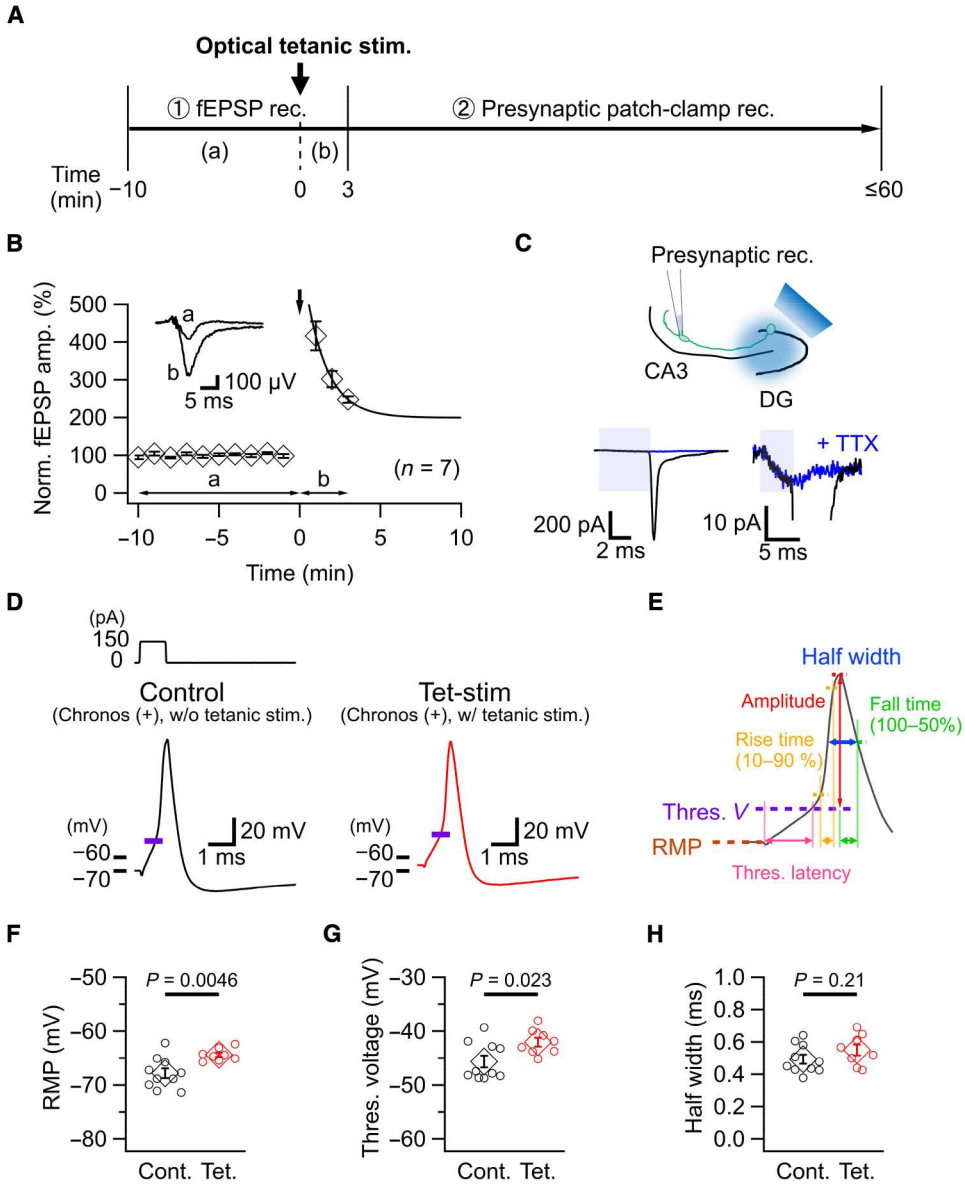

Fig. 2. The effects of the LTP induction protocol on the membrane properties of the hMFBs. (**A**) The scheme of the recording from hMFBs following the optical tetanic stimulation. fEPSPs were recorded (①) for 10 min before (a) and ~3 min after (b) the optical tetanic stimulation (Fig. 1E). Patch-clamp recordings were performed in the following period (≤60 min after the tetanic stimulation; ②). (**B**) The amplitudes of the fEPSPs plotted against the time after the tetanic stimulation (arrow). A solid curve indicates the result of an exponential fitting. fEPSPs before (a) and after the tetanic stimulation (b) are shown in the inset. The data are related to (D) to (H) and fig. S3 (A to E), and *n* indicates the number of slices. (**C**) The scheme of the presynaptic recording in the Chronos-(+) hMFBs (top). An example of a photoevoked current under voltage-clamp condition (black) in response to light illumination at DG (blue shades) is shown (bottom). The response was largely blocked by the application of tetrodotoxin (TTX; 1 μM) (blue), indicating that the response was a spike current originating from an AP in the GC. The enlarged traces (bottom right) highlight Chronos-mediated inward current recorded in the presence of TTX. (**D**) Membrane voltages recorded under current-clamp mode in response to rectangular current injections to the hMFBs (150 pA, 1 ms) without (left, control) and with the tetanic stimulation (right, Tet-stim). Levels of the AP threshold are also shown (purple). (**E**) Various parameters of AP waveforms. RMP, resting membrane potential. (**F** to **H**) RMP (F), threshold voltage (G), and full width at the half maximum (H) of the APs in (D) under the control and Tet-stim conditions. The other waveform parameters are shown in table S1. Statistical significances were assessed with unpaired *t* test.

broadened as the stimulus number increased, but it is unlikely that the broadening is maintained over a minute after the stimulation (fig. S1). We first examined whether tetanic stimulation caused such changes using current-clamp recordings. We injected depolarizing current pulses and elicited APs in both control hMFBs and those after tetanic stimulation (here termed Tet-stim condition; Fig. 2D). Under the control condition, the RMP was −67.8 ± 0.9 mV (control; $n = 10$), a value similar to a previous study (Fig. 2F) (*29*). After the tetanic stimulation, the RMP was depolarized slightly (−64.4 ± 0.4 mV in Tet-stim; $n = 8$), and likewise, the threshold voltage of the AP was positively shifted with little change in threshold latency (Fig. 2, F and G, and table S1; see also fig. S2, A and B, for

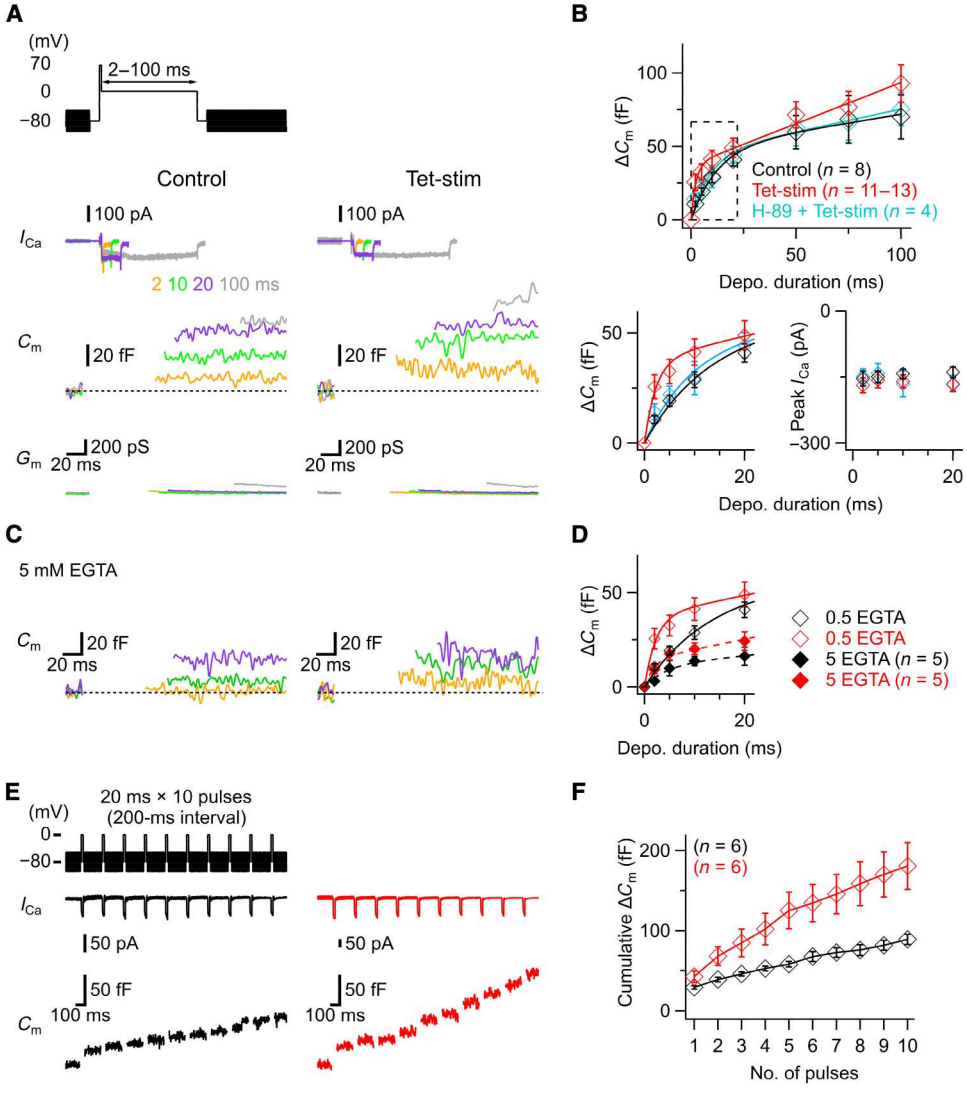

Fig. 3. The LTP induction protocol caused faster time course of cumulative release and faster replenishment of the RRP in the hMFBs, without tightening the coupling distance between Ca^{2+} channels and synaptic vesicles. (**A**) Membrane capacitance measured with sinusoidal voltage before and after the depolarization (70-mV pre-pulse for 2 ms followed by 0-mV test pulse with a duration of 2 to 100 ms; top). Inward Ca^{2+} current (I_{Ca}), membrane capacitance (C_m), and conductance (G_m) are shown. In (A) and (C), responses to the test pulses for 2 (orange), 10 (green), 20 (purple), and 100 ms (gray). In (A), (C), and (E), control (left) and Tet-stim conditions (right). (**B**) C_m increase (ΔC_m) plotted against the test pulse durations (top). ΔC_ms and peak I_{Ca} for 2- to 20-ms pulses are shown (bottom). In (B) and (D) to (F), control (black) and Tet-stim conditions (red) and Tet-stim condition in the presence of 10 μM H-89 (cyan; "H-89 + Tet-stim"). In (B) and (D), lines indicate the fittings of an exponential and a linear function (see table S2 for the fitting results). (**C**) The same set of experiments as (A) was performed with the pipette solution containing 5 mM EGTA. C_ms for 2- to 20-ms pulses are shown. (**D**) ΔC_ms in the presence of 0.5 mM [open; same as (B), bottom left] and 5 mM EGTA (filled) are superimposed. (**E**) I_{Ca} (middle) and C_m (bottom) in response to the repetitive application of constant depolarization to 0 mV for 20 ms (10 times, 200-ms interval; top). (**F**) Cumulative ΔC_ms plotted against the numbers of the repetitive pulses. In (B), (D), and (F), statistical significances were assessed with two-way analysis of variance (ANOVA) (see table S3 for the P values).

the individual data points), implying a change in the membrane conductance below the threshold level. When we injected 500-ms rectangular currents (−10 to 100 pA) and measured steady-state membrane voltages, the voltage changes in response to hyperpolarizing pulses tended to be smaller under the Tet-stim condition than under the control condition, unlike those at the depolarizing pulses, which were almost identical between the conditions (fig. S3, A and B). This result suggested an increase in the shunting conductance at the hyperpolarization, consistent with an enhanced role of HCN channels after LTP induction, as suggested in a previous study (*13*). To examine whether the subthreshold depolarization following the LTP induction (~4 mV) affects the following evoked release, we examined the effect of 10-mV subthreshold depolarization (for 10 s) on the successive release. We have seen no major effect (fig. S4, C to G), although we cannot exclude the possibility that long-term depolarization causes some impact on the release.

When we injected 150-pA current for 1 ms without a holding current, the APs reached a peak (~70 mV from the threshold voltage) with a rise time of ~0.25 ms and showed full width at half maximum of ~0.5 ms and a fall time of ~0.3 ms (Fig. 2, E

and H, and table S1; see also fig. S2C for the individual data points of full width at half maximum). We could not detect significant differences in these parameters between the control and the Tet-stim conditions. Furthermore, changes in the AP waveform and threshold by the tetanic stimulation were not detected, when APs were evoked at the RMP maintained around −80 mV by a holding current (fig. S3, C to E, and table S1). We also tested whether tetanic stimulation influenced APs at the GC soma with somatic current injections, resulting in no significant differences in the AP parameters regardless of whether a holding current was applied (fig. S3, F to K, and table S1). Thus, these results suggest that our LTP induction protocol did not alter the AP waveform.

The LTP induction protocol increased the Pr without changing the RRP size

Next, we examined whether tetanic stimulation affected the RRP size and/or Pr in the RRP by applying membrane capacitance measurements to the hMFBs and quantifying glutamate release. We applied sinusoidal waves (±30 mV, 500 or 1000 Hz) to measure membrane capacitance before and after depolarization in the presence of tetrodotoxin (TTX; 1 μM), a blocker of voltage-gated Na^+ channels, allowing us to measure synaptic vesicle release in response to evoked Ca^{2+} influx as an increase of membrane capacitance (ΔC_ms) caused by synaptic vesicle fusion (Fig. 3A). Note that paired pre- and postsynaptic recording at the MF-CA3 synapses revealed that ΔC_ms and the numbers of released vesicles calculated from excitatory postsynaptic currents (EPSCs) were linearly correlated (fig. S4, A and B), indicating that the release could be quantified by membrane capacitance measurements. We carried out capacitance measurements 15 to 60 min after the LTP induction and compared the results with those in control (Fig. 3; see fig. S6).

Because membrane capacitance could not be measured during the depolarization due to large conductance changes, we measured the capacitance before and after the pulse to quantify the cumulative amounts of release. Thus, the changing duration of the depolarization (0 mV for 2 to 100 ms following predepolarization to +70 mV to activate Ca^{2+} channels maximally; Fig. 3A, top) allowed us to measure the time course of cumulative release (Fig. 3B). In control and Tet-stim hMFBs, the depolarizing pulses triggered Ca^{2+} current with a peak amplitude of ~150 pA on average without a significant difference [Fig. 3B, bottom right; see also fig. S6A (top) for the individual data points]. This indicates that an increase in the presynaptic Ca^{2+} influx is unlikely within the first hour period after LTP induction, consistent with a previous study using the intracellular Ca^{2+} measurements (*30*).

When ΔC_ms were plotted against the pulse durations, ΔC_ms increased as the duration got longer and became saturated around 20 ms under both control and Tet-stim conditions (Fig. 3B and table S2; see also fig. S5). The 20-ms pulse, which can be used for the RRP size estimates, evoked ΔC_m of 40.9 ± 4.1 fF under control ($n = 8$) and 49.9 ± 6.6 fF under Tet-stim condition [$n = 12$; $P = 0.37$, unpaired t test; see also figs. S5B and S6A (middle) for the individual data points]. Because the release time course was somewhat slower under control condition, the RRP might not have been depleted by a 20-ms pulse. Nevertheless, when 20-ms depolarization was applied twice with an interval of 200 ms, the second ΔC_ms was reduced to ~30% of the first one, suggestive of depletion of RRP by a 20-ms pulse (Fig. 3, E and F) (*31*). Moreover, when the external Ca^{2+} concentration was raised to 5 mM under control condition, the time course of cumulative release was faster, and we could separate the RRP depletion and the following replenishment (fig. S5A). In this condition, the estimate of the RRP was similar to that of 2 mM Ca^{2+} (fig. S5B). Together, the data suggested no significant change of the RRP size between control and Tet-stim conditions (~500 vesicles, assuming ~0.1 fF per vesicle; see fig. S4, A and B). On the other side, the time course of cumulative release, an index of vesicular Pr, was much faster under Tet-stim condition. At shorter (<20 ms) pulses, the Tet-stim hMFBs showed larger ΔC_ms than the control ones [Fig. 3B (bottom left) and table S3]. The 2-ms ΔC_m was 2.4 times larger under the Tet-stim condition [$P = 0.020$, unpaired t test; see also fig. S6A (bottom) for the individual data points], an extent similar to the amplification of fEPSPs after the PTP phase (Figs. 1, G and H, and 2B). These results suggested that tetanic stimulation increased Pr of the vesicles within the RRP at the MF-CA3 synapses. The faster time course of cumulative release was not observed in the presence of H-89 [Fig. 3B (bottom left) and table S3; see also fig. S6A (bottom) for the individual data points], indicating that the faster time course of cumulative release after LTP induction was PKA dependent. Together, our data suggest that a higher Pr of the RRP vesicles underlies a PKA-dependent presynaptic LTP at the MF-CA3 synapses.

Faster time course of cumulative release could be caused by tighter spatial coupling between Ca^{2+} channels and synaptic vesicles (positional priming) (*32*). In this case, the sensitivity of release to EGTA would change (*33*–*35*). We measured the membrane capacitance at control and Tet-stim hMFBs under 5 mM EGTA condition and compared the results with those obtained under the 0.5 mM EGTA condition (Fig. 3, C and D). For control hMFBs, we found that raising the EGTA concentration suppressed ΔC_ms, consistent with previous studies (Fig. 3D) (*31*, *32*, *36*). Such suppression was also observed for Tet-stim hMFBs (Fig. 3D), indicating no obvious change in the sensitivity of the release to EGTA. In support, extracellular application during recording of membrane-permeable EGTA (EGTA-AM; 10 or 20 μM) reduced fEPSPs to a similar extent under both the control and the Tet-stim conditions (fig. S7). These results clearly suggest that tighter Ca^{2+} channel-exocytosis coupling is not responsible for mfLTP.

Beyond 20 ms, ΔC_ms showed a slow, linear increase, presumably representing synaptic vesicle replenishment to the RRP (Fig. 3B, top). At these longer pulses, ΔC_m showed a somewhat steeper increase under the Tet-stim condition than the control [Fig. 3B (top) and table S2], implying faster synaptic vesicle replenishment after tetanic stimulation. To resolve vesicle replenishment, we applied repetitive RRP-depleting pulses (20-ms depolarization 10 times with 200-ms intervals) and measured the membrane capacitance (Fig. 3E). ΔC_m was the largest at the first pulse and became constant at later pulses, reflecting depletion of the RRP and subsequent vesicle replenishment. The constant increment was more prominent under the Tet-stim condition (Fig. 3F and table S3; see also fig. S6B for individual data points), supporting faster RRP replenishment after LTP induction.

Increases in the amounts of priming proteins after the LTP induction

If spatial coupling between Ca^{2+} channels and release-ready vesicles does not underlie mfLTP, then fusion competence (molecular priming) (*2*, *37*) could be involved. To get some additional insights in this issue, we performed immunohistochemical quantification of

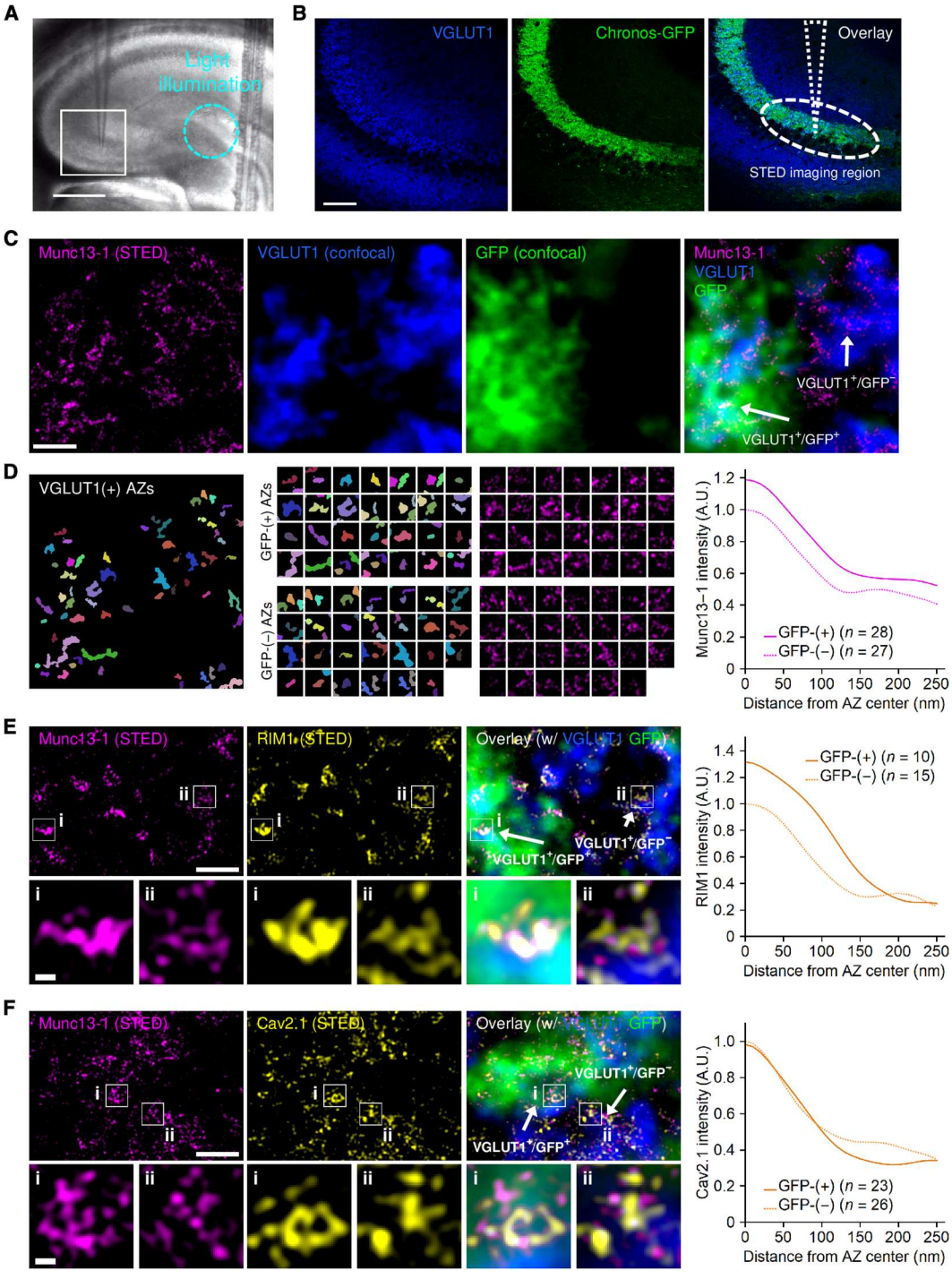

Fig. 4. Immunolabeled Munc13-1, RIM1, and Cav2.1 molecules were visualized by STED microscopy at the hMFBs. (**A**) Location of the light illumination (cyan) and region of interest around the recording electrode (white) are schematically indicated. In (A) to (F), in Tet-stim condition. (**B**) Stratum lucidum in the cryosection processed from the slice that underwent the optical tetanic stimulation. In (B), (C), (E), and (F), Chronos-GFP (green) and VGLUT1 confocal signals (blue). Regions of interest were taken from the area close to the location of the field recording (dashed). (**C**) Munc13-1 signals under STED microscopy (magenta) overlaid with VGLUT1 and Chronos-GFP signals. (**D**) AZs identified by the Munc13-1 STED signals in VGLUT1-(+) regions in (C) (left) were classified by the presence of GFP signals and clipped out one by one (middle left). Munc13-1 STED signals for the individual AZs (middle right) and their mean spatial intensity profiles in the AZs (right) are shown. In (D) to (F), the mean intensities in the GFP-(+) (solid) and GFP-(−) (dashed) AZs in the representative images are plotted against the distances from the centers of the AZs, and the values were normalized by the peak intensities for the GFP-(−) AZs. (**E** and **F**) RIM1 (E) or Cav2.1 (F) (yellow) visualized with Munc13-1 (magenta) under STED microscopy is overlaid with VGLUT1 and Chronos-GFP signals. Rectangular regions in each top image indicate GFP-(+) (i) and GFP-(−) regions (ii), which are cropped and magnified in the corresponding bottom panels. Mean spatial intensity profiles in the AZs are shown (right). AZs were identified by RIM1 (E) or Cav2.1 signals (F). Scale bars, 500 μm (A), 100 μm (B), 1 μm [(C) and top panels in (E) and (F)], and 100 nm [bottom panels in (E) and (F)]. *n* indicates the number of AZs.

synaptic vesicle priming proteins (Munc13-1 and RIM1) (*38*) and the α subunit of the P/Q-type Ca^{2+} channels responsible for glutamate release (Cav2.1; Figs. 4 and 5 and fig. S8) (*39*). We optically induced mfLTP in acute hippocampal slices while recording fEPSPs (Fig. 4A; see also Fig. 1). After establishing mfLTP (recorded for at least 30 min), the slices were rapidly frozen with liquid nitrogen for cryosectioning. We then used the cryosections for immunostaining and precluded the use of cross-linking chemical fixatives (e.g., paraformaldehyde), which limit accessibility of the antibodies to their epitopes in the synaptic molecular complex (*40*), except for the postfixation step (see Materials and Methods). Immunohistochemical labeling of GFP and VGLUT1 (a glutamatergic presynaptic marker) enabled us to identify Chronos-GFP-(+) hMFBs near the location of the field recordings in the stratum lucidum (Fig. 4B). In AZs, molecules are arranged within nanoscopic space below the diffraction limit (*41*, *42*). We therefore used STED microscopy to quantify the proteins localized at AZs. STED microscopy resolved nanoscale subsynaptic structures of

Munc13-1 (Fig. 4, C and D), RIM1 (Fig. 4E), and Cav2.1 (Fig. 4F) in the hMFBs. To quantitatively analyze the amounts of these proteins, we estimated AZ areas from the STED signals by creating binary masks with unsharp masking and image binarization (Fig. 4D; see Materials and Methods) and measured the intensities for the AZs classified according to whether they belonged to the GFP-(+) terminals or not (Figs. 4, D to F, and 5). This allowed us to assess the effect of mfLTP induction on the localization of Munc13-1, RIM1, and Cav2.1 by comparing the signals between GFP-(+) and GFP-(−) hMFBs within the same preparations [Figs. 4, D to F (right). and 5B], thus minimizing potential bias due to experimental and biological variations. The above procedures were also performed for control slices that were incubated in the same manner but had not undergone the tetanic stimulation (Fig. 5A). The cumulative distribution of intensity revealed that the signal intensity of Munc13-1 in GFP-(+) AZs was ~16% stronger than that of the GFP-(−) AZs in Tet-stim preparations [Fig. 5B, left; see also Fig. 4D (right) for the mean intensity profiles in the AZs for the representative data]. Similarly, the signal intensity of RIM1 was ~17% stronger in GFP-(+) AZs than in GFP-(−) AZs in the Tet-stim preparations [Fig. 5B, middle; see also Fig. 4E (right) for the mean intensity profiles in the AZs for the representative data]. Differences in the signal intensities of these proteins were smaller in the control preparations (Fig. 5A, left and middle) and the preparation having undergone the LTP induction in the presence of H-89 (Fig. 5C, left and middle).

For electrophysiological analysis, we have used the slices that were not exposed to the LTP induction protocol as a control. We then calculated the mean signal intensity of Munc13-1 and RIM1 for each slice and compared them among control, Tet-stim, and H-89 + Tet-stim conditions. When we measured the signal intensities in the GFP-(+) AZs normalized to those in the GFP-(−) AZs, Tet-stim preparations showed significantly higher signal intensities of these proteins than control ones. The increased signals were inhibited, at least in part, by H-89 (Fig. 5D, left and middle). Thus, the results suggest that the numbers of Munc13-1 and RIM1 molecules in the AZs are increased by mfLTP induction.

In contrast to the priming proteins, the signal intensity of Cav2.1 in the AZs was little affected by the LTP induction [Fig. 5, A to D (right); see also Fig. 4F (right) for the mean intensity profiles in the AZs for the representative data]. The coupling distance between Munc13-1 and Ca^{2+} channels might determine the efficacy of neurotransmitter release (*43*). We therefore examined whether the distance between Munc13-1 and Cav2.1 was changed after induction of mfLTP by two-color STED imaging analysis (fig. S8). In this analysis, subsynaptic clusters of Munc13-1 and Cav2.1 were estimated by image deconvolution (fig. S8A), and the nearest neighbor (center-to-center) distance between these clusters was quantified in both control and Tet-stim preparations (fig. S8B). The nearest neighbor distance between Munc13-1 and Cav2.1 clusters in the GFP-(+) AZs was similar between control and Tet-stim preparations (median values of 64.7 and 64.9 nm, respectively). These results are consistent with the similar Ca^{2+} channel–vesicle coupling between the control and Tet-stim conditions (Fig. 3, C and D, and fig. S7).

DISCUSSION

The mechanisms of activity-dependent presynaptic LTP remain unclear because of a lack of direct presynaptic recordings. In this study, we examined the mechanisms of presynaptic LTP at the MF-CA3 synapses by combining optogenetic stimulation, direct patch-clamp recordings, and STED microscopy. We first established the induction of activity-dependent LTP using optical stimulations, a widely known type of presynaptic LTP (*10*, *11*). With the aid of GFP-tagged Chronos, we could identify the stimulated terminals. We examined the release mechanism by capacitance measurements. While the RRP size did not change, we observed increased Pr and faster synaptic vesicle replenishment. Moreover, STED microscopy suggested an increase in the numbers of Munc13-1 and RIM1 molecules, showing dynamic changes in the AZ nanostructure during mfLTP.

At MF-CA3 synapses, K^+ channel inactivation progresses during repetitive stimulation and broadens the AP waveform, causing short-term facilitation of glutamate release via increased Ca^{2+} influx (*20*). AP broadening occurs in short-term depolarization-induced potentiation (*44*). Our results suggest that such broadening does not occur upon activity-dependent mfLTP (Fig. 2). RMP was slightly depolarized after the induction (Fig. 2). An enhanced role of HCN currents upon mfLTP [(*13*), but see (*14*)] could be involved, presumably via cAMP elevation, which increases the opening of HCN channels around the RMP (*45*). However, the small change in RMP is possibly insufficient to amplify the release (fig. S4, C to G). More depolarized RMP and lower Ca^{2+} buffering could be necessary to influence subsequent release (*28*, *46*).

STED microscopy has shown that the number of Munc13-1 and RIM1 molecules in AZs increased during mfLTP (Figs. 4 and 5). Both proteins are essential for regulating the RRP size, fusion competence, and vesicle recruitment (*47*–*52*). Because of the multifunctional roles of these proteins, it is difficult to dissect how an increase in the protein number gives rise to functional changes during LTP. Sakamoto *et al.* (*42*) have proposed that the content of Munc13-1 in the AZs determines the release site number and the RRP size in the hippocampal synapses in culture [but see (*53*)]. The RRP size increases during some forms of short-term plasticity such as PTP (*54*). Accordingly, we expected an increase in the RRP size during mfLTP. However, we observed that Pr in the RRP was increased during mfLTP, whereas the RRP size remained the same (Fig. 3). How can we reconcile our electrophysiological and STED results?

The RRP size was estimated to be around 500 vesicles per hMFB by using either depolarizing pulses or Ca^{2+} uncaging method (*21*, *55*). The RRP per AZ is 20 to 30 vesicles, which is much higher than that of hippocampal synapses in culture (*42*). Morphologically, the RRP likely includes not only docked vesicles but also vesicles located within 50 nm from the plasma membrane (*56*, *57*). Therefore, most vesicles within the RRP cannot spatially access Munc13-1 fully, which is essential for fusion competence and, consequently, might become reluctant for release in response to Ca^{2+} influx. We propose that these reluctant vesicles are converted to rapidly releasable ones during mfLTP through recruitment of the Munc13-1/RIM1 complexes (Fig. 6). We anticipate that sufficient Munc13-1 is provided at synapses with high Pr, such as hippocampal synapses in culture, so that most RRP vesicles are fusion-competent. Our results might correspond to the previously formulated "loose versus tight complex" of the release machinery (*2*). In the course

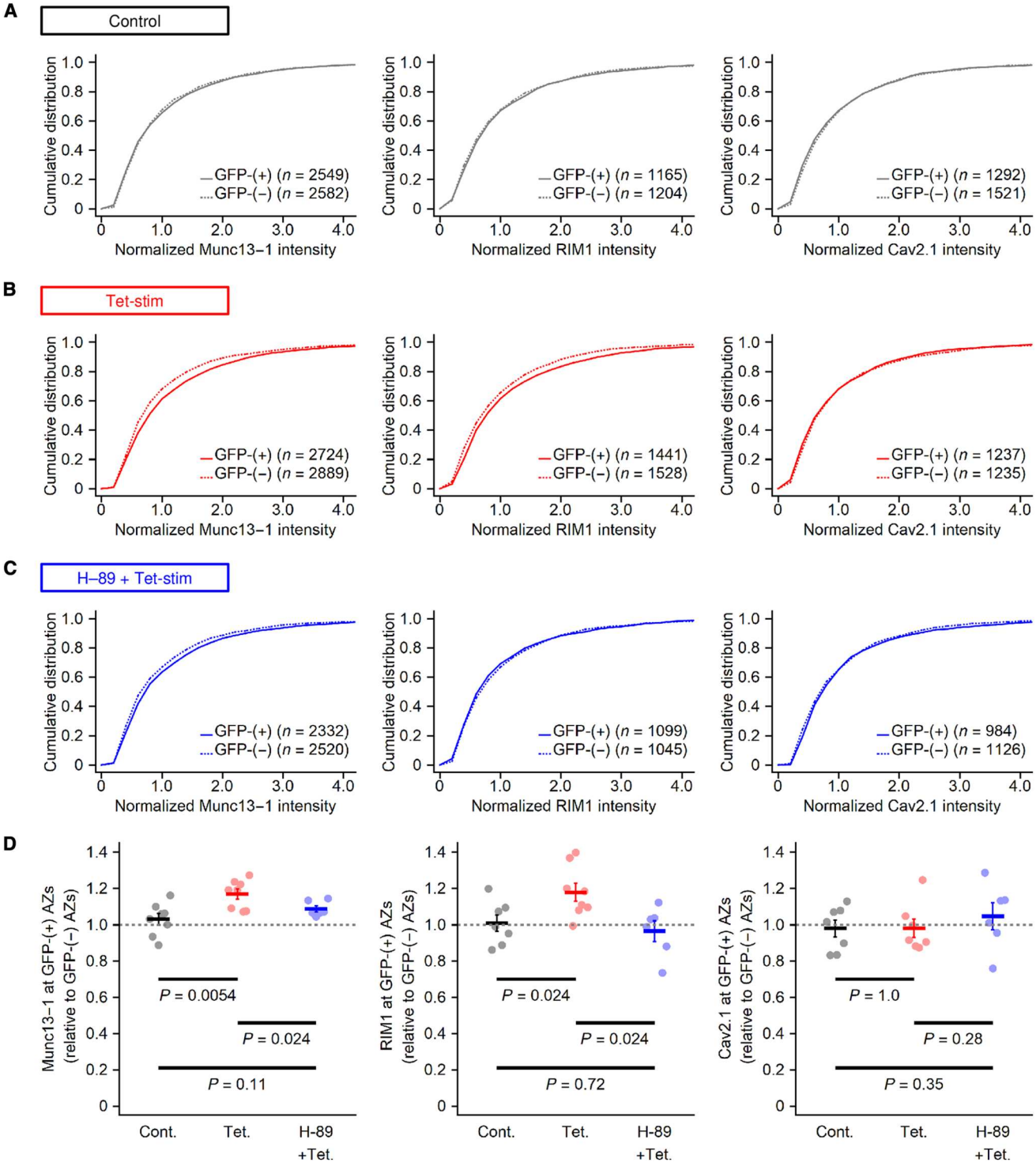

Fig. 5. Signal intensities of Munc13-1, RIM1, and Cav2.1 molecules in the AZs at the hMFBs. (**A** to **C**) Cumulative distributions of intensities of Munc13-1 (left), RIM1 (middle), and Cav2.1 (right) for the GFP-(+) (solid) and GFP-(−) AZs (dashed). The data for the slices under control (A) and Tet-stim conditions (B) and Tet-stim condition in the presence of H-89 (C) are shown. *n* indicates the number of AZs. (**D**) Intensities of Munc13-1 (left), RIM1 (middle), and Cav2.1 (right) in GFP-(+) AZs in preparations under control, Tet-stim, and H-89 + Tet-stim conditions. Each circle represents a mean value of all AZs for each animal. Values were normalized to the mean values for GFP-(−) AZs in the same preparations (gray dashed lines). Statistical significances were assessed using Mann-Whitney *U* test.

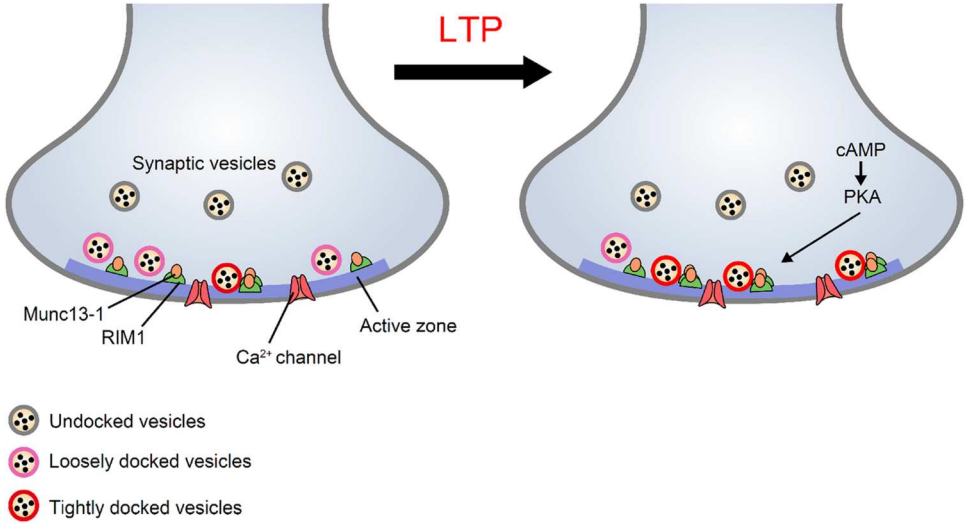

Fig. 6. Working hypothesis of an increase of Pr for vesicles in the RRP during mfLTP. Under the basal condition (**left**), the RRP contains loosely (pink) and tightly docked vesicles (red). After LTP induction (**right**), cAMP/PKA cascade triggers recruitment of Munc13-1/RIM1 complexes in the AZs. This increase of the number of Munc13-1/RIM1 complexes induces the conversion of loosely docked vesicles to tightly docked vesicles, leading to an increase of Pr in the RRP. Note that the shape of the presynaptic terminal is generalized for simplicity.

of a tethered vesicle becoming docked/primed loosely and then tightly at the release site, the sensitivity of fusion to Ca^{2+} influx increases. Our data are in line with a dynamic state within the RRP and a conversion from loose to tight states during mfLTP. A tight state may be unstable at rest but stabilized by the recruitment of Munc13-1/RIM1, which increases fusion competence. Alternatively, the data might be explained by an increased occupancy of vesicles at the preexisting docking site during LTP (*58*). Enhanced vesicle replenishment during mfLTP is consistent with the known role of Munc13-1 in vesicle replenishment under baseline conditions (*51*, *52*).

Our results are also in line with those of previous studies, suggesting distinct mechanisms of forskolin-induced chemical potentiation and physiological activity–dependent LTP. Previous studies have reported that RIM1α and Rab3A, which are important for mfLTP, are not required for chemical potentiation (*16*, *17*). Mechanistically, in contrast to increased fusion competence and vesicle recruitment during mfLTP, pharmacological cAMP/PKA activation increases vesicular Pr by the accumulation of Ca^{2+} channels near release sites on a short-term scale (*32*, *55*). Long-term forskolin incubation results in an increase in the number of vesicles in the RRP and the docked vesicles (*56*, *59*). Differences in the magnitude and spatiotemporal patterns of PKA activation may result in different modes of potentiation.

The present study may explain why Munc13-1 and RIM1 are important for mfLTP (Figs. 4 and 5). Munc13-1 is responsible for tethering and priming of the readily releasable vesicles (*47*, *50*–*52*), which assembles in AZs and forms release sites (*42*, *60*–*62*). Munc13-1 has a domain interacting with RIM1α, and impairment of this interaction inhibits priming (*38*) and diminishes presynaptic LTP at MF-CA3 synapses (*15*). RIM1α is associated with vesicular Rab3, and both proteins contribute to mfLTP (*16*, *17*). Kaeser *et al.* (*63*) showed that the direct modulation of vesicle docking/priming by phosphorylation of RIM1 is not required for mfLTP: Rather, an increase in the number of proteins may be more crucial. Our results imply that these molecules, presumably as a complex, contribute to enhanced priming upon mfLTP, thereby increasing the Pr and replenishment of readily releasable vesicles rather than the RRP size.

Although our study showed the increased intensities of Munc13-1 and RIM1 signals in the AZs after LTP induction, elucidating the underlying molecular mechanism and establishing the causal relationship between the increases of these molecules and the enhanced fusion competence need to be done in further studies. The increased intensity could be mobilization of molecules to the AZs such as insertion of new molecules or transport along plasma membrane to the AZs (*64*). In addition, we used MF synapses as a model system because the synapse shows robust presynaptic LTP and can be accessible with patch clamp. It remains to be seen whether the present results can be extended to presynaptic LTP in other synapses and other forms of plasticity.

MATERIALS AND METHODS

Experimental design

This study has taken three experimental approaches. (i) We expressed photoactivated cation channels together with GFP in GCs via viral injection during stereotactic brain surgery to selectively stimulate MFs of GCs and to induce mfLTP by light (Fig. 1), helping us to identify the hMFBs stimulated by the optical LTP induction. (ii) We applied direct presynaptic patch-clamp recordings to the photosensitive hMFBs to investigate the presynaptic membrane properties (Fig. 2) and transmitter release process (Fig. 3) after induction of LTP. (iii) We quantified AZ molecules in the hMFBs (Figs. 4 and 5) using STED microscopy to reveal the molecular basis of presynaptic LTP.

Ethical approval

All animal experiments were performed in accordance with the guideline of the Japanese Physiological Society and approved by

the animal care committee of Doshisha University and the University of Tokyo.

Viral injection

Female and male Wistar rats (Japan SLC) were subject to a stereotactic brain surgery at postnatal day 10 (P10) or P11. During the surgery, the animal was continuously anesthetized with isoflurane (1.6 to 2.4%) under control of an anesthetic pump (Univentor). AAV (AAV9-Syn-Chronos-GFP, Addgene) was injected using a Hamilton microsyringe (80014, Hamilton) with a beveled 32-gauge needle. The viral solution (0.5 μl) was injected into the DG (relative to bregma; AP: −3.4 mm, ML: +2.6 mm, DV: −2.7 mm) at a rate of 50 nl/min using a microinjection syringe pump (UMP3, WPI). The needle remained at the target site for 5 min before the beginning of the injection and was removed 10 min after the injection.

Slice preparation

P21 to P25 Wistar rats that underwent the surgery were used for analyses. For some experiments without light stimulation (fig. S4), the non-injected hemisphere or non-operated animals were also used. Animals were anesthetized with isoflurane and decapitated. The brain was dissected, as described previously (*65*). Hippocampal slices (thickness of 300 to 400 μm for electrophysiological recordings; 500 μm for immunohistochemistry) were prepared acutely using a linear slicer (VT1200, Leica). The slicing solution contained the following: 87 mM NaCl, 75 mM sucrose, 2.5 mM KCl, 25 mM $NaHCO_3$, 10 mM glucose, 1.25 mM NaH_2PO_4, 0.5 mM $CaCl_2$, and 7 mM $MgCl_2$, oxygenated with 95% O_2 and 5% CO_2. After slicing, the slices were incubated in the slicing solution for 30 min at 37°C and then for 30 min at room temperature. The slices were further incubated for at least 30 min in an external solution for electrophysiological recordings [artificial cerebrospinal fluid (ACSF)]: 125 mM NaCl, 2.5 mM KCl, 25 glucose, 25 mM $NaHCO_3$, 1.25 mM NaH_2PO_4, 0.4 mM ascorbic acid, 3 mM myo-inositol, 2 mM Na-pyruvate, 2 mM $CaCl_2$, and 1 mM $MgCl_2$, oxygenated with 95% O_2 and 5% CO_2. In some experiments, the slices were incubated for at least 30 min in the ACSF with H-89 (10 μM; Cayman). The electrophysiological experiments were performed within 4 hours after slicing.

Electrophysiological experiments

For electrophysiological recordings, the ACSF above was used as an extracellular solution, unless otherwise stated. The slice was transferred to the recording chamber and visualized under an upright microscope (Olympus BX51WI) equipped with a complementary metal-oxide semiconductor camera (IR 2000, DAGE-MTI). The recording ACSF was perfused, and the recording temperature was maintained at 26° to 28°C using a thermoregulator (TC-324C Single Channel Temperature Controller, Warner Instruments) or at room temperature. Chronos-GFP–expressing GCs were activated by a pulse of 470 nm of blue light (duration, 1 to 5 ms) from a light-emitting diode source (M470L4C1, Thorlabs) delivered through a water-immersion 60× objective lens (LUMPlanFLN or LUMPlanFI/IR, Olympus). Recordings were performed using an IPA (Sutter Instruments) or EPC10/2 amplifier (HEKA). Electrical signals were low-pass–filtered at 2.9 or 5 kHz and digitized at 10 kHz for field recordings and 50 kHz for patch-clamp recordings, while membrane capacitance was sampled at 500 or 1000 Hz.

For field potential recordings in response to the light stimulation targeted at DG, the glass pipette filled with NaCl (1 M) was placed at stratum lucidum at a CA3 region. Light intensity and duration were adjusted so that an amplitude of field potential in the baseline became 0.1 to 0.5 mV and remained stable for >10 min. During the recordings, field potentials were monitored every 20 s with a paired pulse (100-ms interval), and the first responses were used for the analyses except for the paired-pulse data analyses. To induce mfLTP, a pair of trains of 125 light pulses at 25 Hz (separated by 20 s) was applied three times every 60 s (Fig. 1E). NBQX (10 μM; Tocris) and D-APV (50 μM; Tocris) were used to block AMPA/kainate and NMDA receptors, respectively (Fig. 1B). DCG-IV (1 μM; Tocris) was applied at the end of the experiments to verify that optically evoked fEPSPs were mediated by MF inputs (*27*). EGTA-AM (10 or 20 μM; AAT Bioquest), a membrane-permeable form of EGTA, was applied extracellularly (fig. S7).

For whole-cell recordings from hMFBs, we targeted the hMFBs right around the fEPSP recording site. Whole-cell recordings were started at least 2 min after the rupture of the membrane. Once whole-cell configuration was achieved from hMFBs, blue light illumination was applied at DG, and hMFBs showing an optically evoked spike current (Fig. 2C) were analyzed as Chronos-(+) hMFBs. hMFBs at stratum lucidum were identified by Ca^{2+} currents and the capacitance increase in response to depolarization. For patch-clamp recordings under Tet-stim condition, field potentials were monitored for ~3 min after the LTP induction [see Fig. 2 (A and B)]. Presynaptic recordings were performed until 60 min after the induction. For current-clamp recordings, potassium gluconate–based solution was used as an intracellular solution: 125 mM K-gluconate, 15 mM KCl, 10 mM Hepes, 5 mM Na_2-phosphocreatine, 4 mM Mg-ATP, 0.3 mM Na-GTP, and 0.2 to 0.5 mM EGTA (pH 7.3 titrated by KOH, 330 mOsm adjusted by sucrose). For presynaptic and postsynaptic voltage-clamp recordings, a cesium gluconate–based solution was used as an intracellular solution: 135 mM Cs-gluconate, 20 mM Tetraethylammonium chloride (TEA-Cl), 10 mM Hepes, 5 mM Na_2-phosphocreatine, 4 mM Mg-ATP, 0.3 mM Na-GTP, and 0.5 mM EGTA (pH 7.3 titrated by CsOH, 330 mOsm adjusted by Cs-gluconate). The intracellular EGTA was raised at 5 mM in Fig. 3 (C and D) and replaced for 1,2-bis(2-aminophenoxy)-ethane-*N*,*N*,*N*′,*N*′-tetraacetic acid (0.2 mM) in fig. S4 (C to G) to mimic physiological Ca^{2+} buffering (*36*). For membrane capacitance measurements, TTX (1 μM; Wako) was added to the recording ACSF. For the paired recordings (fig. S4, A and B), UBP310 (5 μM; Tocris), D-APV (50 μM), and CTZ (0.1 mM; Tocris) were used to block kainate and NMDA receptors and desensitization of AMPA receptors, respectively.

Patch pipettes were made from glass capillaries (BF150-86-10, Sutter Instruments). Pipette resistance was 3 to 8 megohm for field recordings and somatic patch-clamp recordings and 10 to 25 megohm for presynaptic patch-clamp recordings. In some presynaptic recordings, the tip of the pipette was coated with dental wax (UTILITY WAX, GC Corporation) to reduce the pipette capacitance. Series resistance was 30 to 100 megohm for presynaptic voltage-clamp recordings and 5 to 20 megohm for postsynaptic voltage-clamp recordings. It was compensated only for the postsynaptic recordings so that the residual series resistance was below 5 megohm. A bridge balance was electronically compensated for 80 to 90% in the current-clamp recordings in Fig. 2 and fig. S3. Membrane potentials were not corrected for liquid junction

potentials (~10 mV), except for Fig. 2 and figs. S1 to S4, and the related descriptions in the manuscript.

Electrophysiological analyses

Electrophysiological data were analyzed with Igor Pro (mainly version 7) and Excel (Microsoft). For field potential recordings, each data point is the average of three traces (for 1 min) (Figs. 1G and 2B and fig. S7A). For current-clamp analyses in fig. S3 (F to K) and table S1, Chronos-(+) GCs showing membrane resistance below 500 megohm (assessed with an average of >5 pulses of −2 or −5 pA for 500 ms) were considered for the analyses to minimize the contamination of newborn GC neurons (*66*). Threshold currents were determined with current pulses for 1 ms with a step size of 100 pA (GC soma) and 10 pA (hMFBs). Other AP parameters were measured at the suprathreshold current: 200 pA above the threshold current for GC soma and at 150 pA for hMFBs. RMP was measured at 5 to 10 ms before the current injection. Threshold timing was determined as the point where the second derivative of the trace started to increase sharply with a latency behind the pulse onset (threshold latency). An amplitude and a time course of the AP were calculated, as described in Fig. 2E. For current-voltage relationship analyses (fig. S3, A and B), voltages were measured at the last 50 ms during the pulses. Membrane capacitance was measured with the sinusoidal waves (±30 mV, 500 or 1000 Hz). The membrane capacitance after the depolarization was measured as the average over 50 ms at the plateau phase of the capacitance that appeared after the inward tail current because the tail current shifts the phase and biases the capacitance trace (see Fig. 3A). Data for Ca^{2+} current were analyzed and presented, after leak currents were subtracted off-line by the P/5 protocol. The EPSCs were deconvolved with the miniatureEPSC (mEPSC) waveform to estimate the release rates (fig. S4, A and B), assuming no residual currents because of delayed clearance of neurotransmitters (*67*).

Immunohistochemistry

Acute hippocampal slices (500 μm) were prepared as described above. mfLTP was induced by the tetanic light stimulation, as described in Figs. 1 and 4A, and field potentials were monitored every 20 s for at least 30 min after the tetanic stimulation. Some slices were subject to the optical tetanic stimulation in the presence or absence of H-89, and others without the tetanic stimulation were set as control.

The mfLTP-induced or control slices were transferred into a medium (Tissue Freezing Medium, Leica), immediately frozen with liquid nitrogen, and stored at −80°C until use. Then, 10-μm-thick cryosections were sliced with a cryostat (CM1860, Leica) and retrieved on coverslips (Matsunami glass, 25 × 25, no. 1, 0.13 to 0.17 mm). Conventional chemical fixatives (e.g., paraformaldehyde) were not used for the initial fixation, as previously demonstrated for visualization of the AZ molecules (*68*), to obtain better accessibility of the antibodies to their epitopes (*40*). Namely, the retrieved sections were immediately fixed by dehydration with a heat blower for 1 min, while this procedure helps antibodies to permeate into the cell without detergents (*69*). Sections were further fixed with ethanol at −25°C for 30 min and with acetone for 10 min on ice. After rehydration with phosphate-buffered saline (PBS), fixed sections were blocked with 0.3% bovine serum albumin (Nacalai Tesque) in PBS for at least 30 min.

Antibodies were diluted with the blocking solution and reacted with the preparations. Primary antibodies were applied for 3 hours at room temperature and washed twice with the blocking solution. Secondary antibodies were applied for an hour at room temperature and washed twice with the blocking solution and twice with PBS. The immunostained sections were lastly postfixed with 4% paraformaldehyde for 15 min at room temperature and mounted with an antifade mounting medium (ProLong Glass, Thermo Fischer Scientific). Primary antibodies were mouse monoclonal anti–Munc13-1 [1:1000; immunoglobulin G1 (IgG1)] (*42*), rabbit polyclonal anti-RIM1 (1:400; Synaptic Systems), rabbit polyclonal anti-Cav2.1 (1:400; Synaptic Systems), mouse monoclonal anti-GFP (1:1000; IgG2a, Wako), and guinea pig polyclonal anti-VGLUT1 (1:2000; Synaptic Systems). Secondary antibodies were STAR635P (Abberior)–labeled goat anti-mouse IgG1 (Jackson ImmunoResearch), Alexa Fluor 594 (Thermo Fischer Scientific)–labeled donkey anti-rabbit IgG (Jackson ImmunoResearch), Alexa Fluor 488 (Thermo Fischer Scientific)–labeled goat anti-mouse IgG2a (Jackson ImmunoResearch), and DyLight 405 (Thermo Fischer Scientific)–labeled goat anti–guinea pig IgG (Jackson ImmunoResearch).

STED image acquisition and analyses

STED imaging experiments were performed using a TCS SP8 STED 3X microscopy system (Leica) equipped with a 405-nm diode laser, a pulsed white light laser (WLL), a 592-nm STED laser for alignment, a pulsed 775-nm STED laser for depletion, HyD detectors, and a 100× oil immersion objective lens (numerical aperture 1.4). STED images were acquired using the Leica LAS-X software with an image format of 1024 pixels by 1024 pixels, 16-bit sampling, 8-line accumulations, and 11.36-zoom factor, yielding a pixel size of 10 nm. HyD detectors were configured to counting mode with a time gating from 0.5 to 6.5 ns. A 405-nm diode laser was used to excite DyLight405. WLL at 488, 561, and 633 nm were used to excite Alexa Fluor 488, Alexa Fluor 594, and STAR635P, respectively. The 775-nm STED laser power was set to 75 and 100% of maximum power (~500 mW) for depletion of Alexa Fluor 594 and STAR635P, respectively, and delay time was set to 0 to 300 ps. From one cryosection, three to four regions were imaged at CA3 stratum lucidum close to the field recording site (Fig. 4, A and B). For representation and quantification, raw two-color STED images (pixel size of 10 nm) were deconvolved using a Gaussian kernel with a radius of 4 pixels (40 nm).

All data analyses were performed in Mathematica software (ver. 12.0.0; Wolfram). Custom-made scripts (item S1) were used to estimate the AZ area and the signal intensities of AZ proteins in the STED images. To determine the area of AZs, image masks were generated from STED images of AZ proteins by unsharp masking and image binarization (see Fig. 4D). In unsharp masking process, STED images filtered by Gaussian blur with a radius of 40 pixels (400 nm) were subtracted from STED images filtered by Gaussian blur with a radius of 4 pixels (40 nm). The resultant subtracted images were then binarized, and components larger than 100 pixels (0.01 μm^2) were included in the following analysis as image masks for the AZs. Then, the background-subtracted integral of signal intensity of AZ proteins was quantified using the image masks of AZs. The background signal intensity was estimated from nonsynaptic area in the same STED images. Only AZs that show colocalization with confocal VGLUT1 immunofluorescence signals were included in the analysis. Confocal GFP

immunofluorescence signals were used to identify the hMFBs expressing Chronos-GFP. To calculate mean spatial intensity profiles in the AZs of the representative images (Fig. 4, D to F), the signals in each AZ were clipped out into a 500 nm–by–500 nm region so that the center of mass of the AZ was placed at its center, and the cropped images were then averaged for GFP-(+) and GFP-(−) AZs.

For quantification of the distance between Munc13-1 and Cav2.1 clusters in the AZs (see item S2 for the codes), two-color STED images of Munc13-1 and Cav2.1 were deconvolved using a Gaussian kernel with a radius of 40 nm. Image masks of sub-AZ clusters of these proteins were generated from deconvolved STED images by unsharp masking and image binarization. Then, the center of mass of individual clusters was estimated using the image masks, and the nearest neighbor center-to-center distance from Munc13-1 clusters to Cav2.1 clusters were quantified.

Statistics

Statistical analyses were performed in Excel (Microsoft) or Igor Pro (mainly version 7) for electrophysiological analyses and Mathematica for image analyses. Values are shown as average ± SEM in the text, figures, and tables, unless otherwise stated. An individual data point and *n* represent a value for a bouton or a neuron and the number of boutons or neurons, respectively, unless otherwise stated. Paired or unpaired *t* test or two-way analysis of variance (ANOVA) was applied to compare two groups, unless otherwise stated. Difference in variance was tested with *F* test before paired or unpaired *t* test. Only two-tailed *P* values were considered.

Supplementary Materials

This PDF file includes:
Figs. S1 to S8
Tables S1 to S3
Legends for items S1 and S2

Other Supplementary Material for this manuscript includes the following:
Items S1 and S2

View/request a protocol for this paper from *Bio-protocol*.

REFERENCES AND NOTES

1. H. R. Monday, T. J. Younts, P. E. Castillo, Long-term plasticity of neurotransmitter release: Emerging mechanisms and contributions to brain function and disease. *Annu. Rev. Neurosci.* **41**, 299–322 (2018).
2. E. Neher, N. Brose, Dynamically primed synaptic vesicle states: Key to understand synaptic short-term plasticity. *Neuron* **100**, 1283–1291 (2018).
3. R. S. Zucker, Calcium- and activity-dependent synaptic plasticity. *Curr. Opin. Neurobiol.* **9**, 305–313 (1999).
4. R. S. Zucker, W. G. Regehr, Short-term synaptic plasticity. *Annu. Rev. Physiol.* **64**, 355–405 (2002).
5. R. A. Zalutsky, R. A. Nicoll, Comparison of two forms of long-term potentiation in single hippocampal neurons. *Science* **248**, 1619–1624 (1990).
6. P. E. Castillo, Presynaptic LTP and LTD of excitatory and inhibitory synapses. *Cold Spring Harb. Perspect. Biol.* **4**, a005728 (2012).
7. M. Heisenberg, Mushroom body memoir: From maps to models. *Nat. Rev. Neurosci.* **4**, 266–275 (2003).
8. E. R. Kandel, The molecular biology of memory storage: A dialogue between genes and synapses. *Science* **294**, 1030–1038 (2001).
9. R. A. Nicoll, D. Schmitz, Synaptic plasticity at hippocampal mossy fibre synapses. *Nat. Rev. Neurosci.* **6**, 863–876 (2005).
10. M. G. Weisskopf, P. E. Castillo, R. A. Zalutsky, R. A. Nicoll, Mediation of hippocampal mossy fiber long-term potentiation by cyclic AMP. *Science* **265**, 1878–1882 (1994).
11. Y. Y. Huang, E. R. Kandel, L. Varshavsky, E. P. Brandon, M. Qi, R. L. Idzerda, G. S. McKnight, R. Bourtchouladze, A genetic test of the effects of mutations in PKA on mossy fiber LTP and its relation to spatial and contextual learning. *Cell* **83**, 1211–1222 (1995).
12. C. A. Reid, D. B. Dixon, M. Takahashi, T. V. Bliss, A. Fine, Optical quantal analysis indicates that long-term potentiation at single hippocampal mossy fiber synapses is expressed through increased release probability, recruitment of new release sites, and activation of silent synapses. *J. Neurosci.* **24**, 3618–3626 (2004).
13. J. Mellor, R. A. Nicoll, D. Schmitz, Mediation of hippocampal mossy fiber long-term potentiation by presynaptic I_h channels. *Science* **295**, 143–147 (2002).
14. V. Chevaleyre, P. E. Castillo, Assessing the role of Ih channels in synaptic transmission and mossy fiber LTP. *Proc. Natl. Acad. Sci. U.S.A.* **99**, 9538–9543 (2002).
15. Y. Yang, N. Calakos, Munc13-1 is required for presynaptic long-term potentiation. *J. Neurosci.* **31**, 12053–12057 (2011).
16. P. E. Castillo, R. Janz, T. C. Südhof, T. Tzounopoulos, R. C. Malenka, R. A. Nicoll, Rab3A is essential for mossy fibre long-term potentiation in the hippocampus. *Nature* **388**, 590–593 (1997).
17. P. E. Castillo, S. Schoch, F. Schmitz, T. C. Südhof, R. C. Malenka, RIM1α is required for presynaptic long-term potentiation. *Nature* **415**, 327–330 (2002).
18. Y. J. Kaeser-Woo, T. J. Younts, X. Yang, P. Zhou, D. Wu, P. E. Castillo, T. C. Südhof, Synaptotagmin-12 phosphorylation by cAMP-dependent protein kinase is essential for hippocampal mossy fiber LTP. *J. Neurosci.* **33**, 9769–9780 (2013).
19. Y. Ben-Simon, A. Rodenas-Ruano, K. Alviña, A. D. Lam, E. L. Stuenkel, P. E. Castillo, U. Ashery, A combined optogenetic-knockdown strategy reveals a major role of tomosyn in mossy fiber synaptic plasticity. *Cell Rep.* **12**, 396–404 (2015).
20. J. R. Geiger, P. Jonas, Dynamic control of presynaptic Ca^{2+} inflow by fast-inactivating K^+ channels in hippocampal mossy fiber boutons. *Neuron* **28**, 927–939 (2000).
21. S. Hallermann, C. Pawlu, P. Jonas, M. Heckmann, A large pool of releasable vesicles in a cortical glutamatergic synapse. *Proc. Natl. Acad. Sci. U.S.A.* **100**, 8975–8980 (2003).
22. C. Borges-Merjane, O. Kim, P. Jonas, Functional electron microscopy, "Flash and Freeze," of identified cortical synapses in acute brain slices. *Neuron* **105**, 992–1006.e6 (2020).
23. C. Imig, F. J. López-Murcia, L. Maus, I. H. García-Plaza, L. S. Mortensen, M. Schwark, V. Schwarze, J. Angibaud, U. V. Nägerl, H. Taschenberger, N. Brose, B. H. Cooper, Ultrastructural imaging of activity-dependent synaptic membrane-trafficking events in cultured brain slices. *Neuron* **108**, 843–860.e8 (2020).
24. S. Zucca, M. Griguoli, M. Malézieux, N. Grosjean, M. Carta, C. Mulle, Control of spike transfer at hippocampal mossy fiber synapses in vivo by $GABA_A$ and $GABA_B$ receptor-mediated inhibition. *J. Neurosci.* **37**, 587–598 (2017).
25. N. C. Klapoetke, Y. Murata, S. S. Kim, S. R. Pulver, A. Birdsey-Benson, Y. K. Cho, T. K. Morimoto, A. S. Chuong, E. J. Carpenter, Z. Tian, J. Wang, Y. Xie, Z. Yan, Y. Zhang, B. Y. Chow, B. Surek, M. Melkonian, V. Jayaraman, M. Constantine-Paton, G. K.-S. Wong, E. S. Boyden, Independent optical excitation of distinct neural populations. *Nat. Methods* **11**, 338–346 (2014).
26. P. A. Salin, M. Scanziani, R. C. Malenka, R. A. Nicoll, Distinct short-term plasticity at two excitatory synapses in the hippocampus. *Proc. Natl. Acad. Sci. U.S.A.* **93**, 13304–13309 (1996).
27. H. Kamiya, H. Shinozaki, C. Yamamoto, Activation of metabotropic glutamate receptor type 2/3 suppresses transmission at rat hippocampal mossy fibre synapses. *J. Physiol.* **493**, 447–455 (1996).
28. H. Alle, J. R. P. Geiger, Combined analog and action potential coding in hippocampal mossy fibers. *Science* **311**, 1290–1293 (2006).
29. A. Ruiz, E. Campanac, R. S. Scott, D. A. Rusakov, D. M. Kullmann, Presynaptic $GABA_A$ receptors enhance transmission and LTP induction at hippocampal mossy fiber synapses. *Nat. Neurosci.* **13**, 431–438 (2010).
30. H. Kamiya, K. Umeda, S. Ozawa, T. Manabe, Presynaptic Ca^{2+} entry is unchanged during hippocampal mossy fiber long-term potentiation. *J. Neurosci.* **22**, 10524–10528 (2002).
31. R. Miyano, T. Miki, T. Sakaba, Ca-dependence of synaptic vesicle exocytosis and endocytosis at the hippocampal mossy fibre terminal. *J. Physiol.* **597**, 4373–4386 (2019).
32. M. Midorikawa, T. Sakaba, Kinetics of releasable synaptic vesicles and their plastic changes at hippocampal mossy fiber synapses. *Neuron* **96**, 1033–1040.e3 (2017).
33. E. M. Adler, G. J. Augustine, S. N. Duffy, M. P. Charlton, Alien intracellular calcium chelators attenuate neurotransmitter release at the squid giant synapse. *J. Neurosci.* **11**, 1496–1507 (1991).
34. J. G. Borst, B. Sakmann, Calcium influx and transmitter release in a fast CNS synapse. *Nature* **383**, 431–434 (1996).
35. E. Eggermann, I. Bucurenciu, S. P. Goswami, P. Jonas, Nanodomain coupling between Ca^{2+} channels and sensors of exocytosis at fast mammalian synapses. *Nat. Rev. Neurosci.* **13**, 7–21 (2011).

36. N. P. Vyleta, P. Jonas, Loose coupling between Ca^{2+} channels and release sensors at a plastic hippocampal synapse. *Science* **343**, 665–670 (2014).
37. E. Neher, T. Sakaba, Multiple roles of calcium ions in the regulation of neurotransmitter release. *Neuron* **59**, 861–872 (2008).
38. A. Betz, P. Thakur, H. J. Junge, U. Ashery, J. S. Rhee, V. Scheuss, C. Rosenmund, J. Rettig, N. Brose, Functional interaction of the active zone proteins Munc13-1 and RIM1 in synaptic vesicle priming. *Neuron* **30**, 183–196 (2001).
39. P. E. Castillo, M. G. Weisskopf, R. A. Nicoll, The role of Ca^{2+} channels in hippocampal mossy fiber synaptic transmission and long-term potentiation. *Neuron* **12**, 261–269 (1994).
40. E. M. Schneider Gasser, C. J. Straub, P. Panzanelli, O. Weinmann, M. Sassoè-Pognetto, J. M. Fritschy, Immunofluorescence in brain sections: Simultaneous detection of presynaptic and postsynaptic proteins in identified neurons. *Nat. Protoc.* **1**, 1887–1897 (2006).
41. K. S. Y. Liu, M. Siebert, S. Mertel, E. Knoche, S. Wegener, C. Wichmann, T. Matkovic, K. Muhammad, H. Depner, C. Mettke, J. Bückers, S. W. Hell, M. Müller, G. W. Davis, D. Schmitz, S. J. Sigrist, RIM-binding protein, a central part of the active zone, is essential for neurotransmitter release. *Science* **334**, 1565–1569 (2011).
42. H. Sakamoto, T. Ariyoshi, N. Kimpara, K. Sugao, I. Taiko, K. Takikawa, D. Asanuma, S. Namiki, K. Hirose, Synaptic weight set by Munc13-1 supramolecular assemblies. *Nat. Neurosci.* **21**, 41–49 (2018).
43. N. Rebola, M. Reva, T. Kirizs, M. Szoboszlay, A. Lőrincz, G. Moneron, Z. Nusser, D. A. DiGregorio, Distinct nanoscale calcium channel and synaptic vesicle topographies contribute to the diversity of synaptic function. *Neuron* **104**, 693–710.e9 (2019).
44. M. Carta, F. Lanore, N. Rebola, Z. Szabo, S. V. Da Silva, J. Lourenço, A. Verraes, A. Nadler, C. Schultz, C. Blanchet, C. Mulle, Membrane lipids tune synaptic transmission by direct modulation of presynaptic potassium channels. *Neuron* **81**, 787–799 (2014).
45. A. Ludwig, X. Zong, M. Jeglitsch, F. Hofmann, M. Biel, A family of hyperpolarization-activated mammalian cation channels. *Nature* **393**, 587–591 (1998).
46. G. B. Awatramani, G. D. Price, L. O. Trussell, Modulation of transmitter release by presynaptic resting potential and background calcium levels. *Neuron* **48**, 109–121 (2005).
47. I. Augustin, C. Rosenmund, T. C. Südhof, N. Brose, Munc13-1 is essential for fusion competence of glutamatergic synaptic vesicles. *Nature* **400**, 457–461 (1999).
48. Y. Han, P. S. Kaeser, T. C. Südhof, R. Schneggenburger, RIM determines Ca^{2+} channel density and vesicle docking at the presynaptic active zone. *Neuron* **69**, 304–316 (2011).
49. P. S. Kaeser, L. Deng, Y. Wang, I. Dulubova, X. Liu, J. Rizo, T. C. Südhof, RIM proteins tether Ca^{2+} channels to presynaptic active zones via a direct PDZ-domain interaction. *Cell* **144**, 282–295 (2011).
50. N. Lipstein, T. Sakaba, B. H. Cooper, K. H. Lin, N. Strenzke, U. Ashery, J. S. Rhee, H. Taschenberger, E. Neher, N. Brose, Dynamic control of synaptic vesicle replenishment and short-term plasticity by Ca^{2+}-calmodulin-Munc13-1 signaling. *Neuron* **79**, 82–96 (2013).
51. C. Imig, S. W. Min, S. Krinner, M. Arancillo, C. Rosenmund, T. C. Südhof, J. Rhee, N. Brose, B. H. Cooper, The morphological and molecular nature of synaptic vesicle priming at presynaptic active zones. *Neuron* **84**, 416–431 (2014).
52. N. Lipstein, S. Chang, K. H. Lin, F. J. López-Murcia, E. Neher, H. Taschenberger, N. Brose, Munc13-1 is a Ca^{2+}-phospholipid-dependent vesicle priming hub that shapes synaptic short-term plasticity and enables sustained neurotransmission. *Neuron* **109**, 3980–4000.e7 (2021).
53. M. R. Karlocai, J. Heredi, T. Benedek, N. Holderith, A. Lorincz, Z. Nusser, Variability in the Munc13-1 content of excitatory release sites. *eLife* **10**, e67468 (2021).
54. D. Vandael, C. Borges-Merjane, X. Zhang, P. Jonas, Short-term plasticity at hippocampal mossy fiber synapses is induced by natural activity patterns and associated with vesicle pool engram formation. *Neuron* **107**, 509–521.e7 (2020).
55. R. Fukaya, M. Maglione, S. J. Sigrist, T. Sakaba, Rapid Ca^{2+} channel accumulation contributes to cAMP-mediated increase in transmission at hippocampal mossy fiber synapses. *Proc. Natl. Acad. Sci. U.S.A.* **118**, e2016754118 (2021).
56. L. Maus, C. Lee, B. Altas, S. M. Sertel, K. Weyand, S. O. Rizzoli, J. Rhee, N. Brose, C. Imig, B. H. Cooper, Ultrastructural correlates of presynaptic functional heterogeneity in hippocampal synapses. *Cell Rep.* **30**, 3632–3643.e8 (2020).
57. A. Rollenhagen, K. Sätzler, E. P. Rodríguez, P. Jonas, M. Frotscher, J. H. R. Lübke, Structural determinants of transmission at large hippocampal mossy fiber synapses. *J. Neurosci.* **27**, 10434–10444 (2007).
58. T. Miki, G. Malagon, C. Pulido, I. Llano, E. Neher, A. Marty, Actin- and myosin-dependent vesicle loading of presynaptic docking sites prior to exocytosis. *Neuron* **91**, 808–823 (2016).
59. M. Orlando, A. Dvorzhak, F. Bruentgens, M. Maglione, B. R. Rost, S. J. Sigrist, J. Breustedt, D. Schmitz, Recruitment of release sites underlies chemical presynaptic potentiation at hippocampal mossy fiber boutons. *PLOS Biol.* **19**, e3001149 (2021).
60. M. A. Böhme, C. Beis, S. Reddy-Alla, E. Reynolds, M. M. Mampell, A. T. Grasskamp, J. Lützkendorf, D. D. Bergeron, J. H. Driller, H. Babikir, F. Göttfert, I. M. Robinson, C. J. O'Kane, S. W. Hell, M. C. Wahl, U. Stelzl, B. Loll, A. M. Walter, S. J. Sigrist, Active zone scaffolds differentially accumulate Unc13 isoforms to tune Ca^{2+} channel-vesicle coupling. *Nat. Neurosci.* **19**, 1311–1320 (2016).
61. T. Ghelani, S. J. Sigrist, Coupling the structural and functional assembly of synaptic release sites. *Front. Neuroanat.* **12**, 81 (2018).
62. A. M. Walter, M. A. Böhme, S. J. Sigrist, Vesicle release site organization at synaptic active zones. *Neurosci. Res.* **127**, 3–13 (2018).
63. P. S. Kaeser, H. B. Kwon, J. Blundell, V. Chevaleyre, W. Morishita, R. C. Malenka, C. M. Powell, P. E. Castillo, T. C. Südhof, RIM1α phosphorylation at serine-413 by protein kinase A is not required for presynaptic long-term plasticity or learning. *Proc. Natl. Acad. Sci. U.S.A.* **105**, 14680–14685 (2008).
64. M. A. Böhme, A. W. McCarthy, A. T. Grasskamp, C. B. Beuschel, P. Goel, M. Jusyte, D. Laber, S. Huang, U. Rey, A. G. Petzoldt, M. Lehmann, F. Göttfert, P. Haghighi, S. W. Hell, D. Owald, D. Dickman, S. J. Sigrist, A. M. Walter, Rapid active zone remodeling consolidates presynaptic potentiation. *Nat. Commun.* **10**, 1085 (2019).
65. J. Bischofberger, D. Engel, L. Li, J. R. Geiger, P. Jonas, Patch-clamp recording from mossy fiber terminals in hippocampal slices. *Nat. Protoc.* **1**, 2075–2081 (2006).
66. C. Schmidt-Hieber, P. Jonas, J. Bischofberger, Enhanced synaptic plasticity in newly generated granule cells of the adult hippocampus. *Nature* **429**, 184–187 (2004).
67. E. Neher, T. Sakaba, Combining deconvolution and noise analysis for the estimation of transmitter release rates at the calyx of held. *J. Neurosci.* **21**, 444–461 (2001).
68. C. P. Grabner, M. A. Gandini, R. Rehak, Y. Le, G. W. Zamponi, F. Schmitz, RIM1/2-mediated facilitation of Cav1.4 channel opening is required for Ca^{2+}-stimulated release in mouse rod photoreceptors. *J. Neurosci.* **35**, 13133–13147 (2015).
69. E. M. Neuhaus, H. Horstmann, W. Almers, M. Maniak, T. Soldati, Ethane-freezing/methanol-fixation of cell monolayers: A procedure for improved preservation of structure and antigenicity for light and electron microscopies. *J. Struct. Biol.* **121**, 326–342 (1998).

Acknowledgments: We thank E. Neher, S. J. Sigrist, and T. Miki for comments and R. Miyano for technical assistance. We also thank the IRCN Imaging Core and the University of Tokyo Institutes for Advanced Studies for the use of STED microscopy and for assistance. R.F. acknowledges support from the JSPS Overseas Research Fellowship. H.H. acknowledges support from JST, SPRING (JPMJSP2129). **Funding:** This work was supported by JSPS KAKENHI 20KK0171 and 21K15183 (to H.S.); JSPS KAKENHI 20H03358, 21H05701, and 21K19316 (to Y.H.); JSPS KAKENHI 20H03427 (to K.H.); JSPS KAKENHI 20KK0171 and 21H02598 (to T.S.); JSPS Core-to-Core Program A. Advanced Research Networks JPJSCCA20220007 (to T.S.); and JST, PRESTO JPMJPR21E7 (to H.S.). **Author contributions:** Conceptualization: R.F., H.H., H.S., Y.H., K.H., and T.S. Methodology: R.F., H.H., H.S., Y.H., K.H., and T.S. Investigation: R.F., H.H., H.S., Y.H., K.H., and T.S. Writing (original draft): R.F., H.H., H.S., Y.H., and T.S. Writing (review and editing): R.F., H.S., Y.H., K.H., and T.S. **Competing interests:** The authors declare that they have no competing interests. **Data and materials availability:** All data needed to evaluate the conclusions in the paper are present in the paper and/or the Supplementary Materials.

Submitted 10 June 2022
Accepted 23 January 2023
Published 22 February 2023
10.1126/sciadv.add3616

ScienceAdvances

Increased vesicle fusion competence underlies long-term potentiation at hippocampal mossy fiber synapses

Ryota Fukaya, Himawari Hirai, Hirokazu Sakamoto, Yuki Hashimotodani, Kenzo Hirose, and Takeshi Sakaba

Sci. Adv., **9** (8), eadd3616.
DOI: 10.1126/sciadv.add3616

Science Advances (ISSN) is published by the American Association for the Advancement of Science. 1200 New York Avenue NW, Washington, DC 20005. The title *Science Advances* is a registered trademark of AAAS.